



RESEARCH ARTICLE

White matter mean diffusivity correlates with myelination in tuberous sclerosis complex

Jurriaan M. Peters^{1,2,a} , Robbert R. Struyven^{2,a}, Anna K. Prohl², Lana Vasung², Andrija Stajduhar³, Maxime Taquet², John J. Bushman², Hart Lidov⁴, Jolene M. Singh², Benoit Scherrer², Joseph R. Madsen⁵, Sanjay P. Prabhu², Mustafa Sahin⁶ , Onur Afacan² & Simon K. Warfield²

¹Division of Epilepsy and Clinical Neurophysiology, Department of Neurology, Boston Children's Hospital and Harvard Medical School, Boston, Massachusetts

²Computational Radiology Laboratory, Department of Radiology, Boston Children's Hospital and Harvard Medical School, Boston, Massachusetts

³Croatian Institute for Brain Research and Center of Research Excellence for Basic, Clinical and Translational Neuroscience, University of Zagreb, Zagreb, Croatia

⁴Division of Neuropathology, Department of Pathology, Boston Children's Hospital and Harvard Medical School, Boston, Massachusetts

⁵Department of Neurosurgery, Boston Children's Hospital and Harvard Medical School, Boston, Massachusetts

⁶Translational Neuroscience Center, Department of Neurology, Boston Children's Hospital and Harvard Medical School, Boston, Massachusetts

Correspondence

Simon K. Warfield, Computational Radiology Laboratory, Boston Children's Hospital, 300 Longwood Ave, Mailstop BCH3429, Boston, MA 02115. Tel: 857-218-5172; Fax 617-730-4644; E-mail: simon.warfield@childrens.harvard.edu

Funding Information

J. Peters, B. Scherrer, S. Prabhu, M. Sahin, and S. Warfield are supported by NIH R01 NS079788 and U01 NS082320 grants. A. Prohl is supported by Harvard Catalyst | The Harvard Clinical and Translational Science Center (National Center for Research Resources and the National Center for Advancing Translational Sciences, NIH award UL1 TR001102). S. Prabhu is also supported by the Department of Defense W81XWH-11-1-0365. M. Sahin is additionally supported by NIH U54 HD090255 and U54 NS092090 grants. U54 NS092090 is part of the NCATS Rare Diseases Clinical Research Network (RDCRN). RDCRN is an initiative of the Office of Rare Diseases Research (ORDR), NCATS, funded through collaboration between NCATS, NIMH, NINDS, and NICHD. We thank the Harvard Medical School Neurobiology Department and the Neurobiology Imaging Facility for consultation and instrument availability that supported this work. This facility is supported in part by NINDS P30 grant #NS072030.

Received: 8 March 2019; Revised: 18 April 2019; Accepted: 22 April 2019

Annals of Clinical and Translational Neurology 2019; 6(7): 1178–1190

Abstract

Objective: Diffusion tensor imaging (DTI) of the white matter is a biomarker for neurological disease burden in tuberous sclerosis complex (TSC). To clarify the basis of abnormal diffusion in TSC, we correlated ex vivo high-resolution diffusion imaging with histopathology in four tissue types: cortex, tuber, perituber, and white matter. **Methods:** Surgical specimens of three children with TSC were scanned in a 3T or 7T MRI with a structural image isotropic resolution of 137–300 micron, and diffusion image isotropic resolution of 270–1,000 micron. We stained for myelin (luxol fast blue, LFB), gliosis (glial fibrillary acidic protein, GFAP), and neurons (NeuN) and registered the digitized histopathology slides (0.686 micron resolution) to MRI for visual comparison. We then performed colocalization analysis in four tissue types in each specimen. Finally, we applied a linear mixed model (LMM) for pooled analysis across the three specimens. **Results:** In white matter and perituber regions, LFB optical density measures correlated with fractional anisotropy (FA) and inversely with mean diffusivity (MD). In white matter only, GFAP correlated with MD, and inversely with FA. In tubers and in the cortex, there was little variation in mean LFB and GFAP signal intensity, and no correlation with MRI metrics. Neuronal density correlated with MD. In the analysis of the combined specimens, the most robust correlation was between white matter MD and LFB metrics. **Interpretation:** In TSC, diffusion imaging abnormalities in microscopic tissue types correspond to specific histopathological markers. Across all specimens, white matter diffusivity correlates with myelination.

doi: 10.1002/acn3.793

^aThese two authors contributed equally.

Introduction

Tuberous sclerosis complex (TSC) is a genetic neurocutaneous disorder with prominent neurological involvement. Inactivation of *TSC1* or *TSC2* genes leads to pathologically enhanced activity of the mechanistic target of rapamycin (mTOR) pathway, with subsequent disinhibition of protein synthesis and cell growth. In the brain, aberrant cellular proliferation, differentiation, and migration lead to various malformations including cortical tubers which contain cells with an ambiguous phenotype of both astrocytic and neuronal lineage.¹

Diffusion imaging in TSC reveals abnormalities in white matter appearing normal on structural MRI.^{2,3} Fractional anisotropy (FA) and mean diffusivity (MD) measures of major white matter tracts correlate with the neurological phenotype and can be used as a surrogate marker of disease burden.^{4,5} These same DTI metrics change in response to treatment with mTOR inhibitors.^{6,7} Aberrant myelination inhibition has been reported in both neuronal and oligodendrocyte knockout mouse models of TSC, and can be (partially) prevented with early use of mTOR inhibitors.^{8,9} Increased heterotopic and dysplastic neurons has been reported in one of these models, however, and extensive astrocyte pathology is found in tubers and perituber tissue.^{10,11} Thus, while we suspect dysmyelination of the white matter may drive abnormal white matter diffusion in human TSC, it is not known whether astrocytosis or neuronal ectopy are responsible too.

In addition, in patients with TSC undergoing epilepsy surgery, epileptogenic tubers and the perituber rim have an increased MD compared to nonepileptogenic regions.^{12–14} Pathology-imaging correlations are needed, as they could be translated into better detection and delineation of subtle lesions, advance the prediction of histopathology from in vivo MRI, and ultimately improve surgical outcomes.^{15–17}

To elucidate the histopathological basis of diffusion abnormality in TSC, we directly compared quantitative neuropathological data from epilepsy resection specimens to ex vivo high-resolution structural and diffusion imaging data. Here, we focused on myelination, astrocytosis, and neuronal density in the lesional and perilesional tissues of patients with TSC.

Methods

Subjects

Three children with TSC followed in the Multidisciplinary TSC Program at Boston Children's Hospital underwent

epilepsy surgery for refractory seizures in 2015 and 2016. Inclusion criteria included (1) resection performed “en bloc” suitable for imaging and analysis; (2) preoperative diffusion MRI as part of the surgical workup; and (3) diagnosis of TSC by clinical and/or genetic criteria.¹⁸ The study was approved by the institution's IRB, and informed consent was obtained in all participants.

Preoperative MR acquisition

Preoperative MRI consisted of 3T MRI and included both structural imaging and diffusion-weighted imaging, and has been previously described (Data S1).¹⁹

Specimen preparation

Surgical resections were performed “en bloc,” while adhering to current standards of pediatric neurosurgical care. Tissue was then immediately fixed in formalin for 24 h prior to imaging, to prevent tissue deformation and decay (Fig. 1). Next, the tissue was transferred to proton-free Galden[®] perfluoropolyether (Solvay Solexis, Inc., NJ) to avoid susceptibility artifact¹⁵ and ensure no signal in the background during image acquisition.

While fixation of tissue alters tissue diffusion profiles, the principal eigenvector of the tensor is clearly defined in ex vivo tissue, with good directional correspondence to in vivo data.^{20,21} The Computational Radiology Laboratory has previously optimized acquisition methods for ex vivo brain diffusion-weighted imaging.²²

Ex vivo MR acquisition

3 Tesla MRI acquisitions were performed on Siemens Skyra scanner with 64-channel head coil and a 7 mm loop coil. 7 Tesla MRI acquisitions were performed on Bruker BioSpec 70/30 system with a surface coil, as detailed in the Data S1.

Isotropic resolution for structural imaging ranged from 137 to 300 micron and for diffusion imaging was 1000 micron, 270 micron, and 750 micron for specimens 1, 2, and 3, respectively. T1w, T2w, FA, and MD images were processed on the in-house developed Computational Radiology imaging toolkit.

Figure 2 illustrates the location of the resected regions in the preoperative MRI, and compares the in vivo images to ex vivo imaging, and to gross pathology, for orientation purposes. Due to the relatively low 2.5 × 2.5 × 2.5 mm resolution of clinically acquired in vivo diffusion images, only visual comparison with high-resolution ex vivo images

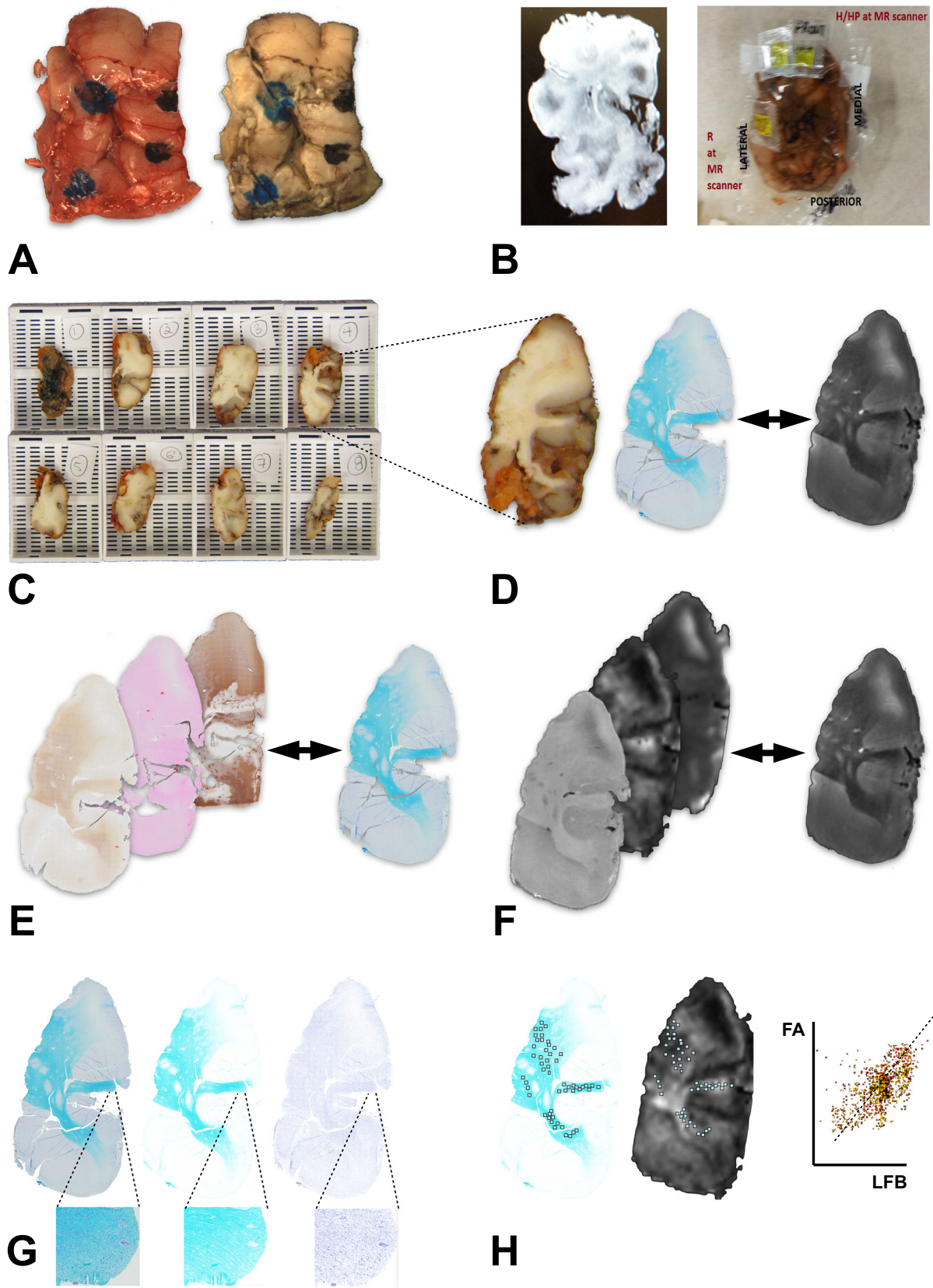


Figure 1. Procedure for comparison of ex vivo histopathology and imaging. (A) Gross resection specimen fresh and after fixation. The blue ink marks the cortical surface. (B) During imaging, potassium pills are placed on the specimen for orientation. A screenshot was made from the scanner display for reference. (C) Block sectioning is done at an orientation that approaches one of the imaging planes. (D) A high-resolution slide, digitized at 0.686 micron, is registered to a high-contrast ex vivo MR T2 image at 137 micron resolution. (E) Pathology slides are registered to the reference pathology slide. (F) All imaging sequences are also registered to the reference image. (G) With color deconvolution, the primary color of interest is extracted from the digitized pathology slide (left). In this case, the luxol fast blue (LFB) is isolated from cresyl violet in an 8-bit monochrome image at the same resolution (middle). The cellular nuclei form a separate image (right), better visible at the higher magnification image inserts. (H) Multiple ROIs are now colocated in corresponding areas of interest in the histopathology and diffusion images. A sample colocalization of intensity values is shown.

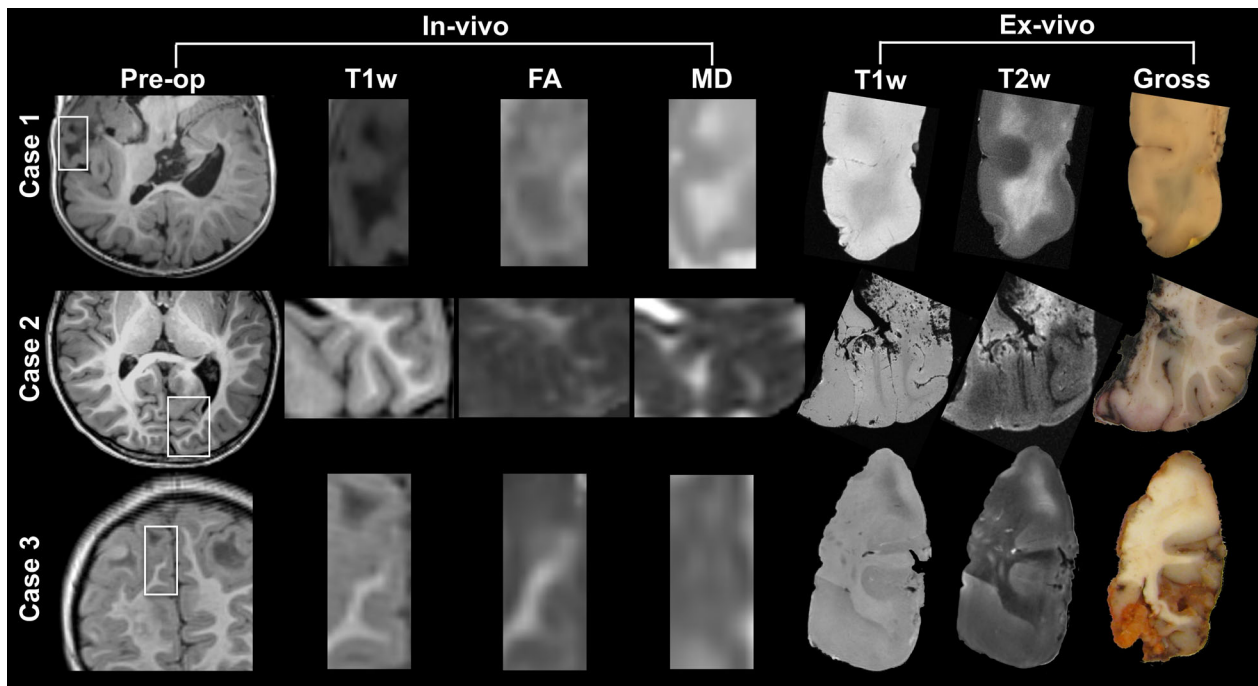


Figure 2. Preoperative imaging and orientation of resection specimens. Resection regions are highlighted in the white rectangle in the preoperative images. Magnified frames of T1-weighted (T1w), fractional anisotropy (FA), and mean diffusivity (MD) are shown, and compared to the ex vivo images on the right. Note that the imaging plane may be inverted and manipulated to match the ex vivo cutting plane and histopathology slide; for example, case 1 is a *pseudo-axial* plane, and images may be inverted along any axis. *Pre-op* preoperative MRI; *T1w* T1-weighted MRI; *T2w* T2-weighted MRI; *FA* fractional anisotropy; *MD* mean diffusivity.

was done. Similarly, given complex and variable orientation of the specimen in different scanners, we did not attempt to reorient the gradient directions, and thus limited the analysis to the magnitude of tensor metrics. More detail can be found in the Data S1.

Blocking specimen, conventional and immunostaining, digitization

Once imaged, the neuropathologist (HL) blocked the specimen with a thickness of 3–7 mm, accounting for the orientation of acquired MR images (Fig. 1). Tissue was embedded in paraffin using a Leica Peloris tissue processor. Sections were cut at 6 microns (except LFB,

at 13 microns) using the Leica RM2255 microtome. Conventional stains were done on a Roche Ventana automated stainer, and immunostaining was done using a Roche BenchMark XT platform with manufacturer protocols optimized for CNS tissue. The following stains were used: Hematoxylin and eosin (H&E; Ventana, Tucson, AZ), Luxol fast blue (LFB; Histo-Chem, Inc., Jefferson, AR), and immunostaining with glial fibrillary acidic protein (GFAP; Dako, Cambridge, MA, polyclonal, 1:1000) and NeuN neuronal stain (NeuN; Chemicon, Temecula, CA, monoclonal, 1:1000). Whole slide digitization took place on an Olympus VS-120 Whole Slide Scanner, at 10 \times magnification at 0.686 micron resolution.

Postprocessing, alignment

MRI slices were compared to digitized histological slides by visual comparison at first, based on anatomical landmarks, tissue edges, and artifacts.^{23,24} Neuropathology registration to the 3D MRI volume was performed with the Histolozee tool from the Penn Image Computing and Science Lab (picsl.upenn.edu). The remaining histology slides were nonrigidly aligned to the reference slide with ImageJ (Fig. 1), using anatomical landmarks on the edge of the specimen.²⁵ Note that 3D reconstruction of histology is outside of the scope of this paper.

All ex vivo MR images including diffusion data were registered to the reference isotropic T1w or T2w structural data series, with rigid and nonrigid registration using a block matching paradigm, to compensate for residual distortion.²⁶

Histopathology and MRI registration

In ImageJ, histology images were color deconvoluted to extract the stain of interest, and obtain optical density measures of LFB and GFAP.^{24,27} Neuronal density and size within each ROI was calculated with an automated cell-count in NeuN-stained histological sections as previously described.²⁸ On the basis of previous work, and if present in the sample, we selected regions of interest (ROIs) in white matter not adjacent to the tuber (“white matter”), transitional tissue between white matter and tuber (“perituber white matter”), and tuber.^{19,29}

A minimum of 100 ROIs were selected, with variable surface area but each encompassing multiple pixels, to assure accuracy and stability of findings.³⁰ The ROIs together formed tissue-specific masks at the resolution of the digitized histopathology slide. Further details can be found in the Data S1.

Statistical analysis

Three statistical analyses were done to address three different questions:

- 1 In each specimen, regional differences between the histological (optical density of GFAP and LFB, density of neurons) and DTI scalars in the four tissue types were evaluated using the Student t-test with estimationstats.com software.
- 2 Also in each specimen, colocalization was done to study correlations between imaging and histopathology metrics. Details on ImageJ's colocalization function (imagej.net/coloc_2) are found in the Data S1.
- 3 Across all three specimens, linear mixed models (LMM) were used to assess consistent associations between tissue type and histopathology. LMM are an

extension of simple linear models which allow for both fixed and random effects. A fixed effect is a parameter that does not vary (an unknown constant) which affects the prediction of the dependent variable. A random effect is nonconstant parameter that introduces systemic variation in the model. Finally, data in the LMM has a hierarchical structure which means that there are clusters of data which are not independent from each other. For more details, please see the Data S1 for a brief layman's explanation of the model.

In the current work, the dependent variable is the tissue type or diffusion metric, the fixed effects (covariates) are the quantitative histopathology measures and the age of subject, and the random effect is the subject. The hierarchy represents the organization of the tissue types, that is, we assumed that the tissue types appear in order from outside (cortex) to inside (tuber, perituber, and then white matter). We opted for this structure as some of the tissue types are hybrid, for example, the perituber tissue is a transitional tissue type between tuber and white matter, and carries histopathological and diffusion imaging features of both.

The parameter estimates of the fixed effects represent the average effect on the dependent variable (e.g., FA) of a one-unit change in a covariate (e.g., LFB), with other covariates held constant, that is, representing the overall effect of LFB on FA across the specimens. Furthermore, the categorical predictors for cortex, tuber, and perituber are calculated with the white matter as a reference group. For example, perituber tissue has a coefficient of -17.15 for FA, confidence interval -26.56 to -7.74, which means that the mean FA in perituber tissue is 17.15 units lower compared to the mean FA of the white matter.

First, linear mixed models were used to assess associations between tissue type and histopathology:

$$\text{Tissue type} = OD^{GFAP} + OD^{LFB} + \text{neuronal density} + \text{age} + \text{subject}$$

Here, tissue type (tuber, perituberal white matter, cortex, and white matter) was the dependent variable; age, GFAP, LFB, and neuronal density were introduced as covariates, and subject as a random factor.

Second, the associations between each DTI metric with histopathology values in each tissue type, adjusted for age and subject, were studied in a similar model:

$$\text{DTI metric} = \text{tissue type} + OD^{GFAP} + OD^{LFB} + \text{neuronal density} + \text{age} + \text{subject}$$

Here, the tissue type (tuber, perituberal white matter, cortex, and white matter) was inserted as a factor; age, GFAP, LFB, and neuronal density as covariates, and

Table 1. Patient data

Case	Sex	Age at onset/surgery	Presurgical workup	Resection site and type	Outcome class ¹
1	Female	0.1/1.0 year	L temporal	partial lateral lobectomy	Engel III ²
2	Female	1.2/6.5 year	L occipital	occipital lobectomy	Engel III
3	Male	1.8/6.2 year	L frontal to right temporal	frontopolar lesionectomy	Engel IV ²

¹Engel Ia, seizure free since surgery; Engel IIIa, worthwhile seizure reduction; Engel IVb, no appreciable change. See text for case details.

²Case 1 became seizure free with a second surgery, extending the prior resection site, and Case 3 became seizure free with vigabatrin.

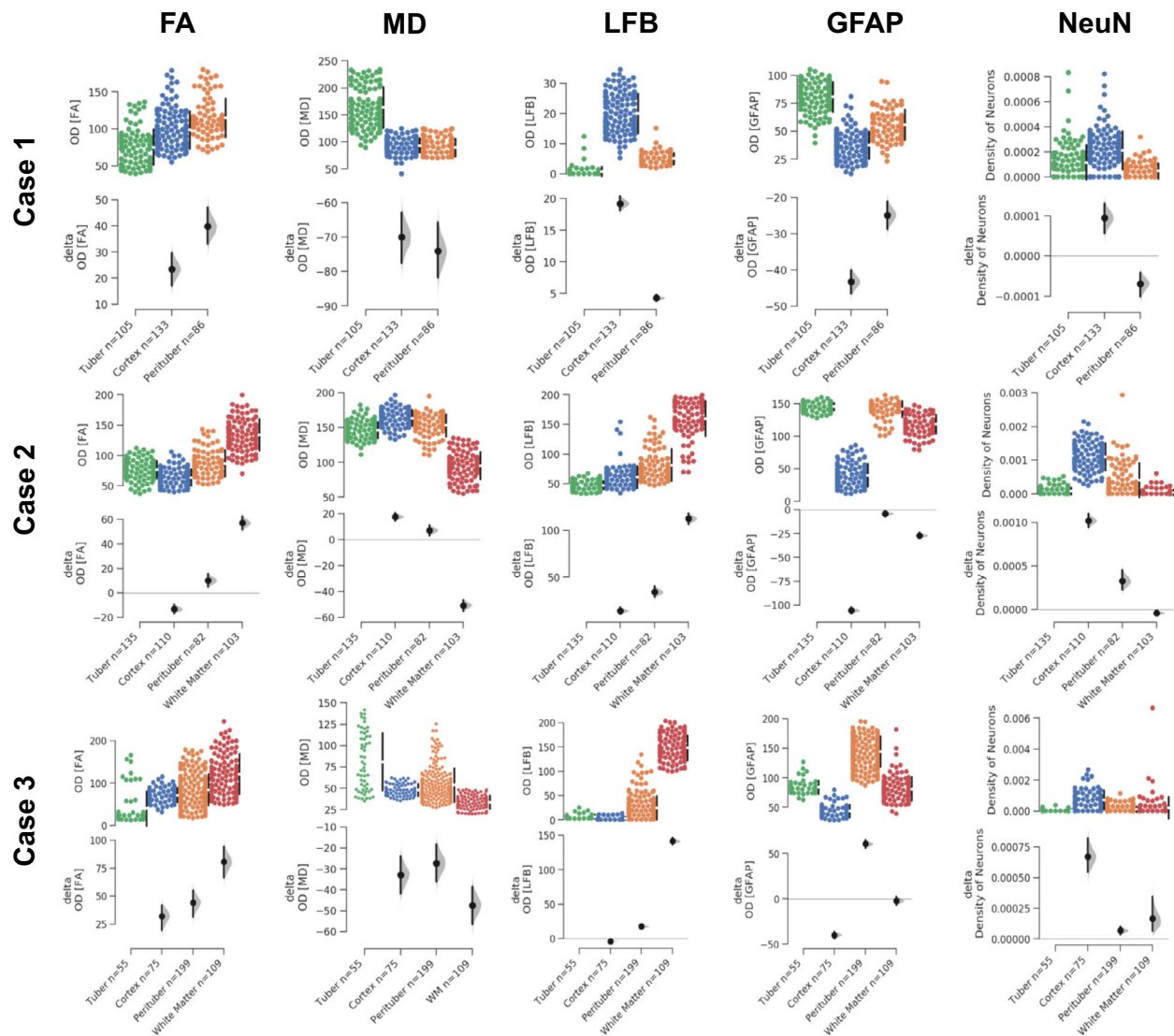


Figure 3. Cumming plots of DTI and neuropathology metrics. Raw ROI data of mean DTI scalars (FA, MD), of optical density (GFAP and LFB stains), and neuronal density (NeuN stain) are shown for tuber (green) and cortex (blue), perituber (orange), and white matter (red) tissue types. For each tissue type, summary measurements (mean \pm standard deviation) are shown as gapped lines, and the number of ROIs is indicated on the x-axis. Below each scatterplot the mean differences with the shared control (tuber) are plotted as bootstrap sampling distributions. The mean difference is depicted as a dot; the 95% confidence interval is indicated by the ends of the vertical error bar, and the filled gray curve represents the distribution of the effect size. FA fractional anisotropy; MD mean diffusivity; LFB luxol fast blue; GFAP glial fibrillary acidic protein; NeuN neuronal nuclei stain; OD optical density.

Table 2. Parameter estimates for linear mixed model for tissue type (cortex, tuber, perituber, white matter)

Parameter	Estimate	95% Confidence Interval		P-value ¹
		Lower Bound	Upper Bound	
Intercept	1.2227	-8.1118	10.5571	0.3460
Age	-0.1242	-1.9027	1.6544	0.5420
Mean LFB	0.0139	0.0133	0.0146	0.0000*
Mean GFAP	0.0119	0.0110	0.0128	0.0000*
Neuronal Density	-190.6483	-274.1398	-107.1568	0.0000*

¹Linear mixed model with tissue type as a factor, age, density of neurons, OD of GFAP and LFB as covariates, and subject as a random factor. Statistically significant P-values of ≤ 0.05 are marked with*.

subject as a random factor. P-values < 0.05 were considered significant, after correction for multiple comparisons.

Results

Patient data

Table 1 shows the main clinical characteristics of the patients.

Visual inspection of neuropathology and MRI

In all modalities, we identified a gradual tissue transition from white matter to perituber tissue, and then to tuber lesion, as previously described.¹⁹ Microscopically small satellite lesions, referred to as *microtubers*,³¹ are evident

both on the registered microscopy slides and on corresponding high-resolution ex vivo images (Figs. S1 and S2).

Specimen 1 revealed an extensive subcortical tuber burden in the temporal lobe, and no white matter myelination at age 1, resulting in only faint background LFB uptake in the cortex and homogenous uptake of GFAP across cortex and tuber tissue.

Quantification of neuropathology and MRI metrics

For diffusion MRI measures, tubers had significantly lower FA compared to the perituber tissue, cortex, and white matter – and conversely the MD was typically highest in tubers, followed by cortex, perituber tissue and the white matter. Case 2, however, had a lower FA (and higher MD) of the cortex and perituber white matter than tuber tissue (Fig. 3).

For the histopathological metrics, LFB optical density was lowest in tubers, higher in perituber white matter, and maximum in more remote white matter (Cases 2 and 3, not Case 1). LFB uptake in the cortex was variable. GFAP optical density was highest in the tubers, then in perituber white matter, followed by white matter. Neuronal count (NeuN) was highest in the cortex compared to tuber and perituber tissues, but no consistent pattern was found between other tissue types (Fig. 3). Neuronal size did not differ in the tissue types (data not shown).

Composite LMM analysis across all specimens revealed that with increasing distance from the cortex, via tuber and then perituber tissue to the white matter, the OD of the GFAP and LFB increased, whereas the density of neurons decreased (Table 2). Likewise, increasing distance from the cortex was associated with an increase in FA and a decrease in MD (Table 3).

Table 3. Parameter estimates for linear mixed models of MD and FA

Parameter	FA				MD			
	Estimate	95% Confidence Interval		P-value ¹	Estimate	95% Confidence Interval		P-value ¹
		Lower Bound	Upper Bound			Lower Bound	Upper Bound	
Intercept	112.9008	103.1775	122.6241	0.0000	86.8769	-801.7890	975.5428	0.4360
Age	-7.4141	-8.4031	-6.4252	0.0000*	-0.2783	-173.2993	172.7428	0.9870
Mean LFB	0.2664	0.2024	0.3304	0.0000*	-0.0384	-0.1052	0.0284	0.2600
Mean GFAP	0.2077	0.1425	0.2730	0.0000*	-0.1519	-0.2076	-0.0962	0.0000*
Neuronal Density	-3332.2716	-7662.2571	997.7140	0.1310	14563.1374	10872.6685	18253.6064	0.0000*
Cortex	-16.2705	-25.5324	-7.0086	0.0010*	14.3930	5.2292	23.5568	0.0020*
Tuber	-39.2181	-48.9224	-29.5139	0.0000*	30.2334	21.5909	38.8760	0.0000*
Perituber	-17.1500	-26.5585	-7.7415	0.0000*	59.6041	49.9442	69.2641	0.0000*
White Matter	0 ²				0 ²			

¹Linear mixed model with tissue type as a factor, age, density of neurons, OD of GFAP and LFB as covariates, and subject as a random factor.

²This parameter is set to zero because it is redundant. Statistically significant P-value of ≤ 0.05 are marked with*.

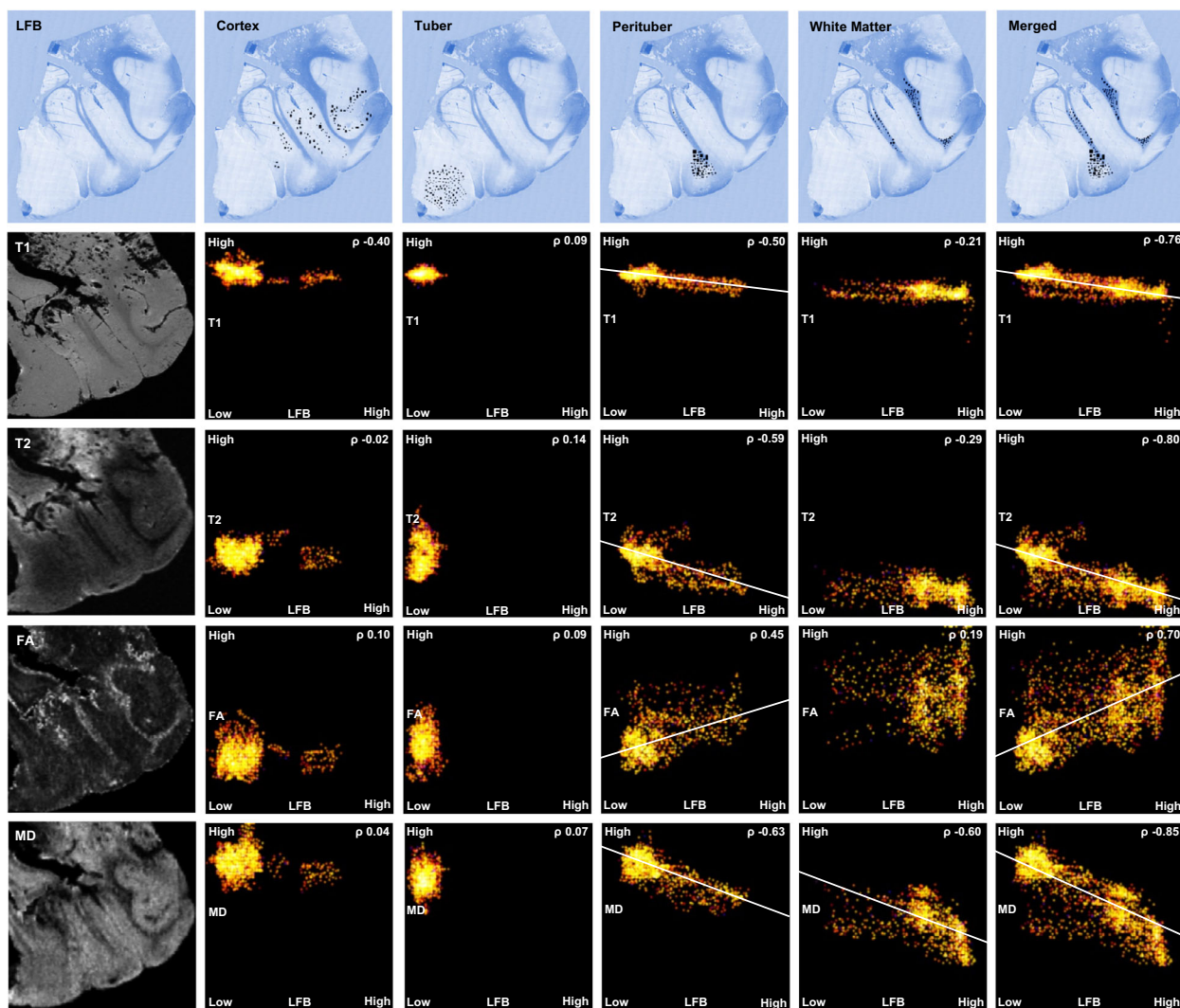


Figure 4. Example Case 2: Colocalization analysis of histopathology (LFB stain, after color deconvolution) and ex vivo MRI. In the left column, T1-weighted and T2-weighted ex vivo structural images and diffusion imaging. On the top row, the regions of interest (ROIs) are placed in the four tissue types: Cortex, tuber, perituber, and white matter. In the last column, two tissue types (perituber and white matter) are merged, yielding a wider distribution of optical density values. In the graphs, the colored dots indicate intensity histograms, and the hotter colors indicate more overlap between MRI metrics (y-axis) and histopathology optical density values (x-axis). Spearman's Rho correlations are listed, and regression lines are shown for higher values for illustration purposes. Note that perituber and white matter tissues at times form two different local maxima in the intensity histograms, for example, in the merged white matter mask. This means these tissue types have different mean signal intensities. *LFB* luxol fast blue; *T1* T1-weighted; *T2* T2-weighted; *FA* fractional anisotropy; *MD* mean diffusivity.

Colocalization and linear mixed modeling of neuropathology and MRI metrics

LFB and diffusion metrics

In the colocalization analysis, the LFB optical density measures in the white matter and perituber white matter correlated negatively with T2 and MD images, as illustrated in Figure 4. By merging the ROIs for the white matter and perituber white matter, the distribution of

both LFB and MD values was wider, and we found a consistent negative correlation in each specimen. LFB and FA had a positive but less consistent correlation in these tissue types.

The LMM analysis demonstrated a positive correlation between FA and optical densities LFB, and the inverse was found for MD (Table 3). AD and RD did not correlate with LFB, so we could not assess what was driving the correlation with FA (Table S1).

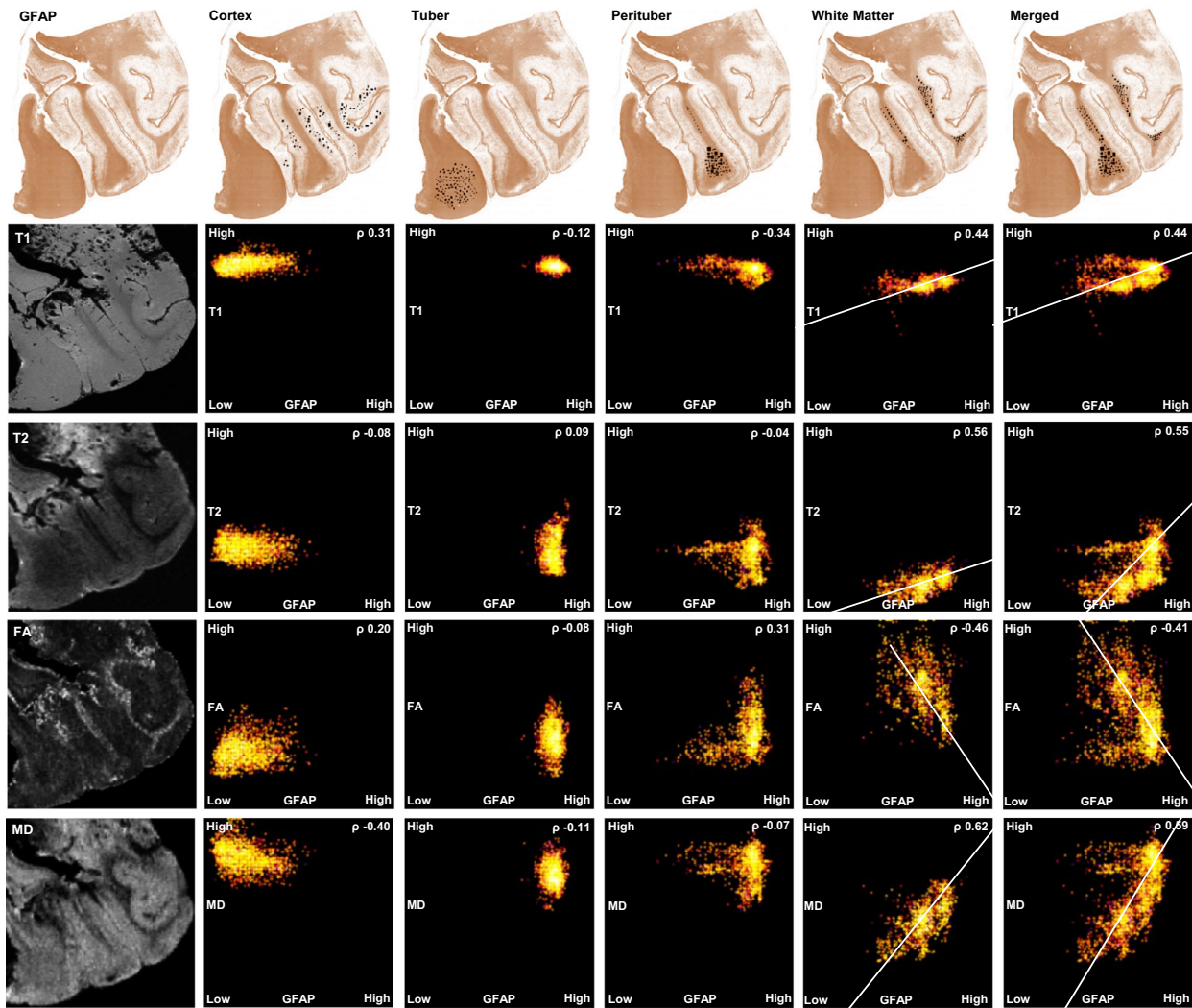


Figure 5. Example Case 2: Colocalization analysis of histopathology (GFAP stain, after color deconvolution) and ex vivo MRI. In the left column, T1-weighted and T2-weighted ex vivo structural images and diffusion imaging. On the top row, the regions of interest (ROIs) are placed in the four tissue types: Cortex, tuber, perituber, and white matter. In the last column, two tissue types (perituber and white matter) are merged, yielding a wider distribution of optical density values. In the graphs, the colored dots indicate intensity histograms, and the hotter colors indicate more overlap between MRI metrics (y-axis) and histopathology optical density values (x-axis). Spearman's Rho correlations are listed, and regression lines are shown for higher values for illustration purposes. Note that perituber and white matter tissues at times form two different local maxima in the intensity histograms, for example, in the merged white matter mask. This means these tissue types have different mean signal intensities. Legend: GFAP glial fibrillary acidic protein; T1 T1-weighted; T2 T2-weighted; FA fractional anisotropy; MD mean diffusivity.

GFAP and diffusion metrics

In the colocalization analysis, the GFAP optical density measures in the white matter correlated positively with T2 and MD images, as illustrated in Figure 5. GFAP and FA had negative but weaker and less consistent correlation in the white matter. No consistent correlation pattern was present in other tissue types.

LMM of DTI metrics showed, in contrast, a positive correlation between FA and optical density of GFAP, and

the inverse was found for MD (Table 3) – driven by both AD and RD (Table S1).

NeuN and diffusion metrics

For NeuN, the use of neuronal count rather than an optical density measure precluded the colocalization analysis. LMM analysis of DTI metrics showed no correlation between FA and neuronal density, but MD positively correlated with neuronal density (Table 3).

Discussion

In this study, we have correlated 3T and 7T high-resolution ex vivo structural and diffusion MRI of surgical resection specimens with quantitative neuropathology in TSC. Our protocol included an initial matching of pathology and MRI based on visual review of anatomy,^{23,24} followed by more objective rigid and nonrigid registration of the specimens and MRI, which is computationally complex but reproducible.¹⁶

Myelination

On visual inspection and quantitatively, LFB optical density measures were highest in white matter, lower in perituber tissue, and lowest in tubers. This gradual change in myelination is in line with ill-defined rather than discrete borders of tuber pathology,¹⁹ and with reduced myelin in dysplastic tissue.^{24,32,33}

In both the colocalization analysis and in the LMM, in both the white matter and perituber white matter, quantitative LFB measures correlated with FA, and inversely with MD metrics, suggesting decreased myelination is present in areas with increased diffusion.

In clinical imaging data in children with TSC, we have previously shown DTI measures of the white matter reflect the neurological disease burden. Presence of neurological comorbidities like refractory epilepsy, neurodevelopment and autism spectrum disorder are cumulatively associated with a decreased FA and an increased MD of the corpus callosum.⁵ Moreover, DTI changes are seen in response to treatment with mTOR inhibitors in patients with TSC, but the underlying mechanism is not known.^{6,7} The current work suggests this could represent alterations in myelination, as also seen in rodent models.^{8,9,34,35}

Mechanistically, possible explanations for increased diffusion with reduced myelination are numerous, and include aberrant oligodendrocyte maturation and dysmyelination, reduced numbers of myelinated axons, increased heterotopic cells, enlarged extracellular space from neuronal loss or edema, and demyelination.^{8,9,24,32,33,35–37}

In FCD type IIb, which histopathologically and genetically overlaps with TSC, many such features were seen in an ex vivo MRI-histopathology study. T2w hyperintensity in the white matter was associated with myelinated fiber loss, high balloon cell density, and dysmyelination. Reduced and dysmorphic oligodendrocytes were also found in these specimens.²⁴ In a mouse model with an inactivated *Tsc2* gene in oligodendrocyte precursors, similar decreases in myelinated axon density, myelin thickness, and oligodendrocyte numbers have been reported.⁸ Although a direct histopathology-to-MRI comparison was

not made, ex vivo MRI of the callosal white matter in this model showed a reduced FA,⁸ similar to our work in human patients.⁵

Clinically, our patients had highly refractory epilepsy which warranted epilepsy surgery. Such uncontrolled and recurrent seizures could constitute an additional “hit” to the already abnormal myelinogenic process in TSC. Longitudinal imaging in children with TSC has revealed diffusion changes and cyst-like degeneration of tuber tissue which could also represent superimposed injury from seizures over time.^{6,19,38} In FCD type II, seizure effects have not been seen consistently; one study reported a correlation between epilepsy severity or duration and white matter pathology intensity,³³ whereas others did not find this correlation.²⁴ A more recent study of 20 epilepsy resection specimens from patients with FCD type II did not report changes in tissue injury markers (including gliosis) in perilesional tissue and white matter with recurrent seizures.³⁹ Our sample was too small to assess a contribution of seizure severity.

Astrocytosis

On visual inspection and quantitatively, reactive astrocytosis, represented by GFAP optical density measures, was typically higher in the tubers than in perituber tissue and white matter, and was lowest in the cortex – consistent with the predominance of glial cells in tuber and perituber tissue,⁴⁰ and with reports of increased GFAP in FCD-related white matter.¹⁵

Next, in the colocalization analysis of the white matter, GFAP optical density correlated with T2w intensity and with MD. This is different than reported in a study of five resection specimens in FCD, where GFAP correlated with T2w intensity in the cortex, but not in the white matter.¹⁵ In a different study of temporal lobe epilepsy, GFAP also did not correlate with white matter T2w intensity, or with FA and MD values.^{16,41} The differences with our work could be due to a primary role of astrocyte pathology in TSC.^{11,40} In our specimens, obtained from the correlation of GFAP with MD likely represents extension of tuber pathology into the white matter,^{19,29,31} or effects from recurrent seizures (see above). Clinically, the implications of excessive gliosis in TSC could be in the rational design of antiepileptogenic trials, and diffusion imaging could demonstrate target engagement of such targeted therapies.

For tuber and perituber tissue, in the colocalization analysis the GFAP did not consistently correlate with MD or FA. The round shape of tuber data in the intensity histograms (Fig. 5), shows tubers are relatively homogeneous even at this high resolution, with limited variability in both diffusion metrics and GFAP density; as a result, correlations are low.

In the LMM, however, we found a negative correlation between MD and GFAP, and positive correlation between FA and GFAP. We suspect this is a spurious effect from statistical modeling. In all cases, the cortex had the lowest level of gliosis, and the perituber tissue had more gliosis than the adjacent white matter. Case 1 did not have any white matter and in Case 3 the tuber was largely acellular (low gliosis). Thus, in the composite LMM model there appeared to be a low-to-high gliosis gradient from cortex to tuber to perituber and then to white matter.

Neurons

The positive association between MD and neuronal density in the LMM likely reflects the presence of abundant cortical neurons, a limited quantity of neurons in the white matter, and a variable and intermediate neuronal count in the tuber and perituber tissues. In a neuropathology study of resection specimen from children with TSC to examine glutamate receptor expression, variations in neuronal size were reported.⁴² In our sample, we did not study specific neuronal subpopulations in such detail, and there were no consistent differences in neuronal size between the tissue types.

Limitations and future directions

Several limitations decrease the scope of this work. First, only limited conclusions can be drawn from the small number of resection specimens. The wide age range of patients at different maturational stages of myelination rendered findings instable across specimen. The RD and AD did not correlate consistently with neuropathology across specimens, preventing any conclusions about which diffusion direction was driving MD abnormality. Overall, MD was a more robust metric than FA, as previously reported in our longitudinal diffusion imaging study of TSC, too.⁶

Second, in epilepsy surgery, a good surgical outcome (Engel Class I and II) is considered strong evidence for successful resection of the epileptogenic zone.⁴³ Our poor outcomes prevent us from making inferences about epileptogenic versus nonepileptogenic tubers. Case 2 underwent invasive monitoring, and reactive pathology from surgically implanted hardware could not be differentiated from seizure-related astrocytosis.^{15,16,41}

Finally, comparison with healthy (postmortem) control white was lacking. For intraspecimen consistency, however, we sampled each specimen with multiple ROIs in each tissue type, and analyzed tissue types both separately and combined. In the future, ultrastructural assessment of fiber and oligodendrocyte density and cellular quantification of glial subtypes would complement this work.^{15,44,45}

Acknowledgments

We are indebted to our patients for their participation, and to Boston Children's Hospital MRI technical staff members, for their diligent assistance with data acquisition. The authors thank Michelle Ocaña of the HMS Neurobiology Imaging Facility for microscope training and advice on imaging and analysis, and Meera Modi for critical reading of the manuscript.

Conflict of Interests

None. The authors report no disclosures or conflicts of interest relevant to this work.

Author Contributions

JP, RS, AP, LV, AS, MT, JB, JS, BS, SP, and MS designed and coordinated the study, executed the imaging and slide digitization, registration, and performed the analysis, and contributed to editing and writing the manuscript. HL is responsible for the histopathology aspects, not including quantification. JM provided the specimen and assisted with marking and orientation of the specimen. OA, BS, and SW directed MR image acquisition and processing, assisted in data interpretation, and edited the manuscript.

References

1. Ess KC. The neurobiology of tuberous sclerosis complex. *Semin Pediatr Neurol* 2006;13:37–42.
2. Arulrajah S, Ertan G, Jordan L, et al. Magnetic resonance imaging and diffusion-weighted imaging of normal-appearing white matter in children and young adults with tuberous sclerosis complex. *Neuroradiology* 2009;51:781–786.
3. Makki MI, Chugani DC, Janisse J, Chugani HT. Characteristics of abnormal diffusivity in normal-appearing white matter investigated with diffusion tensor MR imaging in tuberous sclerosis complex. *AJNR Am J Neuroradiol* 2007;28:1662–1667.
4. Peters JM, Sahin M, Vogel-Farley VK, et al. Loss of white matter microstructural integrity is associated with adverse neurological outcome in tuberous sclerosis complex. *Acad Radiol* 2012;19:17–25.
5. Baumer FM, Peters JM, Clancy S, et al. Corpus callosum white matter diffusivity reflects cumulative neurological comorbidity in Tuberous Sclerosis Complex. *Cereb Cortex* 2018;28:3665–3672.
6. Peters JM, Prohl A, Kapur K, et al. Longitudinal effects of everolimus on white matter diffusion in tuberous sclerosis complex. *Pediatr Neurol* 2019;90:24–30.

7. Tillema JM, Leach JL, Krueger DA, Franz DN. Everolimus alters white matter diffusion in tuberous sclerosis complex. *Neurology* 2012;78:526–531.
8. Carson RP, Kelm ND, West KL, et al. Hypomyelination following deletion of Tsc2 in oligodendrocyte precursors. *Ann Clin Transl Neurol* 2015;2:1041–1054.
9. Meikle L, Talos DM, Onda H, et al. A mouse model of tuberous sclerosis: neuronal loss of Tsc1 causes dysplastic and ectopic neurons, reduced myelination, seizure activity, and limited survival. *J Neurosci* 2007;27:5546–5558.
10. Meikle L, Pollizzi K, Egnor A, et al. Response of a neuronal model of tuberous sclerosis to mammalian target of rapamycin (mTOR) inhibitors: effects on mTORC1 and Akt signaling lead to improved survival and function. *J Neurosci* 2008;28:5422–5432.
11. Wong M, Crino PB. Tuberous sclerosis and epilepsy: role of astrocytes. *Glia* 2012;60:1244–1250.
12. Chandra PS, Salamon N, Huang J, et al. FDG-PET/MRI coregistration and diffusion-tensor imaging distinguish epileptogenic tubers and cortex in patients with tuberous sclerosis complex: a preliminary report. *Epilepsia* 2006;47:1543–1549.
13. Jansen FE, Braun KP, van Nieuwenhuizen O, et al. Diffusion-weighted magnetic resonance imaging and identification of the epileptogenic tuber in patients with tuberous sclerosis. *Arch Neurol* 2003;60:1580–1584.
14. Yogi A, Hirata Y, Karavaeva E, et al. DTI of tuber and perituberal tissue can predict epileptogenicity in tuberous sclerosis complex. *Neurology* 2015;85:2011–2015.
15. Reeves C, Tachrount M, Thomas D, et al. Combined Ex Vivo 9.4T MRI and quantitative histopathological study in normal and pathological neocortical resections in focal epilepsy. *Brain Pathol* 2016;26:319–333.
16. Eriksson SH, Free SL, Thom M, et al. Correlation of quantitative MRI and neuropathology in epilepsy surgical resection specimens—T2 correlates with neuronal tissue in gray matter. *NeuroImage* 2007;37:48–55.
17. Madan N, Grant PE. New directions in clinical imaging of cortical dysplasias. *Epilepsia* 2009;50(Suppl 9):9–18.
18. Northrup H, Krueger DA. International tuberous sclerosis complex consensus g. tuberous sclerosis complex diagnostic criteria update: recommendations of the International tuberous sclerosis complex consensus conference. *Pediatr Neurol* 2012;2013:243–254.
19. Peters JM, Prohl AK, Tomas-Fernandez XK, et al. Tubers are neither static nor discrete: Evidence from serial diffusion tensor imaging. *Neurology* 2015;85:1536–1545.
20. Miller KL, McNab JA, Jbabdi S, Douaud G. Diffusion tractography of post-mortem human brains: optimization and comparison of spin echo and steady-state free precession techniques. *NeuroImage* 2012;59:2284–2297.
21. Miller KL, Stagg CJ, Douaud G, et al. Diffusion imaging of whole, post-mortem human brains on a clinical MRI scanner. *NeuroImage* 2011;57:167–181.
22. Scherrer B, Afacan O, Stamm A, et al. Optimized magnetic resonance diffusion protocol for ex-vivo whole human brain imaging with a clinical scanner, Proc. SPIE 9412, Medical Imaging 2015: Physics of Medical Imaging, 94122U, 2015.
23. Eriksson SH, Free SL, Thom M, et al. Reliable registration of preoperative MRI with histopathology after temporal lobe resections. *Epilepsia* 2005;46:1646–1653.
24. Zucca I, Milesi G, Medici V, et al. Type II focal cortical dysplasia: Ex vivo 7T magnetic resonance imaging abnormalities and histopathological comparisons. *Ann Neurol* 2016;79:42–58.
25. Schindelin J, Arganda-Carreras I, Frise E, et al. Fiji: an open-source platform for biological-image analysis. *Nat Methods* 2012;9:676–682.
26. Taquet M, Scherrer B, Commowick O, et al. A mathematical framework for the registration and analysis of multi-fascicle models for population studies of the brain microstructure. *IEEE Trans Med Imaging* 2014;33:504–517.
27. Ruifrok AC, Johnston DA. Quantification of histochemical staining by color deconvolution. *Anal Quant Cytol Histol* 2001;23:291–299.
28. Štajduhar A, Džaja D, Judaš M, Lončarič S. Automatic detection of neurons in NeuN-stained histological images of human brain. *Physica A: Statistical Mechanics and its Applications*, 2019.
29. Ruppe V, Dilsiz P, Reiss CS, et al. Developmental brain abnormalities in tuberous sclerosis complex: a comparative tissue analysis of cortical tubers and perituberal cortex. *Epilepsia* 2014;55:539–550.
30. Eriksson SH, Free SL, Thom M, et al. Methodological aspects of 3D and automated 2D analyses of white matter neuronal density in temporal lobe epilepsy. *Neuropathol Appl Neurobiol* 2006;32:260–270.
31. Marcotte L, Aronica E, Baybis M, Crino PB. Cytoarchitectural alterations are widespread in cerebral cortex in tuberous sclerosis complex. *Acta Neuropathol* 2012;123:685–693.
32. Muhlechner A, Coras R, Kobow K, et al. Neuropathologic measurements in focal cortical dysplasias: validation of the ILAE 2011 classification system and diagnostic implications for MRI. *Acta Neuropathol* 2012;123:259–272.
33. Shepherd C, Liu J, Goc J, et al. A quantitative study of white matter hypomyelination and oligodendroglial maturation in focal cortical dysplasia type II. *Epilepsia* 2013;54:898–908.
34. West KL, Kelm ND, Carson RP, et al. Myelin volume fraction imaging with MRI. *NeuroImage* 2018;182: 511–521.
35. Ercan E, Han JM, Di Nardo A, et al. Neuronal CTGF/CCN2 negatively regulates myelination in a mouse model of tuberous sclerosis complex. *J Exp Med* 2017; 214:681–697.

36. Thom M, Sisodiya S, Harkness W, Scaravilli F. Microdysgenesis in temporal lobe epilepsy. A quantitative and immunohistochemical study of white matter neurones. *Brain* 2001;124:2299–2309.
37. Carson RP, Van Nielen DL, Winzenburger PA, Ess KC. Neuronal and glia abnormalities in Tsc1-deficient forebrain and partial rescue by rapamycin. *Neurobiol Dis* 2012;45:369–380.
38. Chu-Shore CJ, Frosch MP, Grant PE, Thiele EA. Progressive multifocal cystlike cortical tubers in tuberous sclerosis complex: Clinical and neuropathologic findings. *Epilepsia* 2009.
39. Rossini L, Garbelli R, Gnatkovsky V, et al. Seizure activity per se does not induce tissue damage markers in human neocortical focal epilepsy. *Ann Neurol* 2017;82:331–341.
40. Sosunov AA, Wu X, Weiner HL, et al. Tuberous sclerosis: a primary pathology of astrocytes? *Epilepsia* 2008;49(Suppl 2):53–62.
41. Lockwood-Estrin G, Thom M, Focke NK, et al. Correlating 3T MRI and histopathology in patients undergoing epilepsy surgery. *J Neurosci Methods* 2012;205:182–189.
42. Talos DM, Kwiatkowski DJ, Cordero K, et al. Cell-specific alterations of glutamate receptor expression in tuberous sclerosis complex cortical tubers. *Ann Neurol* 2008;63:454–465.
43. Brodbeck V, Spinelli L, Lascano AM, et al. Electroencephalographic source imaging: a prospective study of 152 operated epileptic patients. *Brain* 2011;134:2887–2897.
44. Muhlebner A, van Scheppingen J, Hulshof HM, et al. Novel Histopathological Patterns in Cortical Tubers of Epilepsy Surgery Patients with Tuberous Sclerosis Complex. *PLoS ONE* 2016;11:e0157396.
45. Sosunov AA, McGovern RA, Mikell CB, et al. Epileptogenic but MRI-normal perituberal tissue in Tuberous Sclerosis Complex contains tuber-specific abnormalities. *Acta Neuropathol Commun* 2015;3:17.

Supporting Information

Additional supporting information may be found online in the Supporting Information section at the end of the article.

Figure S1. Qualitative comparison of histopathology and ex vivo MRI of Case 2

Figure S2. Qualitative comparison of histopathology and ex vivo MRI of Case 3

Table S1. Parameter estimates for linear mixed model of RD and AD

Data S1. Methods